A new approach to DEM simulation of sand production

Yifei Cui*, Alireza Nouri, Dave Chan, Ehsan Rahmati

Department of Civil and Environmental Engineering, University of Alberta, AB, T6G 1H9, Canada

ABSTRACT:

This paper presents a model for the investigation of sandstone degradation and sand production mechanisms coupled with fluid flow analysis using the Discrete Element Method (DEM). The model was used to investigate the effects of in-situ stresses and flow rate on sand production.

We developed a linked DEM-fluid flow model for sanding analysis. The model calculates seepage forces and applies them on solid particles in the DEM model. The model accounts for permeability and porosity changes due to sandstone deformation and sand production. The DEM model was verified against poro-elastoplastic analytical solutions. Subsequently, the model was used for sanding simulation from a block-shaped sample under different far-field stress and pressure conditions. The boundary stresses and fluid pressures were varied to study their influence on sandstone degradation and sand production.

The creation of a borehole in a solid block resulted in the development of uniform or V-shape breakouts around the borehole. The failure zone around the borehole expanded after the application of fluid flow and sand grain detachments. Fluid flow was observed to influence the size and mode of failure in the breakout zone and sand production. Boundary stress dominated the sanding response at higher boundary stress conditions. However, much lower sanding occurred under higher boundary stresses but low boundary fluid pressures. High tangential stresses around the borehole caused by high confining stress resulted in strong frictional interlocking that alleviated sand production. Massive sanding was observed at lower far-field stress but higher boundary pore pressure.

Keywords: Discrete Element Method; Fluid flow coupling; Permeability and porosity alterations; Sand production

1. Introduction

Sanding is the production of formation sand driven by de-cementation of the formation sand around the borehole and the flow of reservoir fluid during the oil recovery process. Problems associated with sand production include erosion of pipelines and surface facilities, wellbore intervention costs, and environmental impacts. Large amounts of sand production in a short period of time may clog up wells, damage well equipment, and destabilize wellbores due to loss of materials (Climent et al., 2014). On the other hand, controllable sand production may increase wellbore productivity and reduce wellbore completion costs (Saucier, 1974). Therefore, understanding sand production mechanisms and the ability to predict and manage the rate of sand production are important.

While both experimental and analytical models of sand production are necessary to understand the phenomenon, numerical models are essential for realistic predictions (Rahmati et al., 2013a). Sand production in oil wells is often analyzed using continuum models. However, the process of sandstone de-cementation involving the development of cracks and micro-cracks in the inter-granular bonding material and grain detachments due to seepage forces are intrinsically problems of a discontinuum and are not compatible with the assumptions of continuum mechanics.

An alternative approach that overcomes some of these limitations is adopting the discrete element method (DEM) for this problem. In order to apply the DEM in the sanding problem, it is necessary to calculate fluid flow and pore water pressure in the discontinuum. In this work, we linked a three-dimensional DEM model

*Corresponding author
E-mail address: cui4i@ualberta.ca (Y. Cui)

with fluid flow calculations to simulate sand production. Coupling the DEM model with continuum fluid computation allows the simulation of solid-fluid interactions.

The use of DEM for simulating solid-fluid interactions has been attempted in a few research studies in the past. Tsuji et al. (1993) developed a solid-fluid coupling scheme to simulate fluidized beds. In their study, the fluid phase was discretized into elements larger than the particle sizes. They calculated the average values of the pore pressure and fluid velocity within each grid block. The fluid force was calculated in each block and applied to each discrete particle. Chan (1993) solved the fluid flow equations using the finite difference method and coupled the continuum fluid flow problem with DEM solids. Chan and Tipthavonnukul (2008) developed a coupling method to investigate the hydro-transport of solid particles in pipelines or open channels. They solved the continuity equation and the Navier-Stokes equations using a finite volume scheme with a pressure correction algorithm. One difficulty with the above approaches is that the solutions of the mass balance and three momentum equations for fluid flow are computationally demanding.

Majority of previous studies (e.g. Boutt et al., 2011; Quadros et al., 2010; Cook et al., 2004) involve 2D discrete models. Two-dimensional models offer a good qualitative insight. However, they are not suitable for application in general 3D reality. Further, solid particles in 2D models are bar-shaped, and the loading conditions in the direction normal to the model plane are not realistic. It cannot model plane stress or plane strain conditions.

Grof et al. (2009) developed a 3D DEM-fluid flow model. Their study was focused on a small-scale phenomenon involving only a few particles. Cheung (2010) developed a 3D DEM coupled with 1D fluid flow for the simulation of sand production. However, they neglected the gradual change in the wellbore geometry and the concomitant variation of fluid flow directions near the continuously changing cavity face.

Climent et al. (2014) developed a 3D DEM-fluid flow model by coupling DEM and Computational Fluid Dynamics (CFD). The simulation is focused on the effect of different far field boundary stress and outer boundary pore pressure conditions. The results were consistent with analytical solution by Risnes et al. (1982). However, their simulations were limited to a certain boundary stress and pore pressure conditions. Furthermore, they did not consider permeability change due to sand production near the wellbore.

Van Den Hoek et al. (2000) developed an analytical solution to calculate the failure of the initial cavity in a hollow cylinder sample and compared with experimental results. They studied the influence of the far field stress and pressure drawdown on the failure of the initial cavity. By calculating the maximum allowable fluid flow rate, they concluded that the primary role of fluid flow in sand production is the transport of loose sand resulting from compression failure rather than failure of the intact sandstone itself. The tensile failure can only take place around small cavities in weak sandstones, or in case of very highly localized pore pressure gradient.

In this paper, we propose a new approach to simulate sand production by using 3D DEM-fluid flow model. We use an innovative method for the calculation of seepage forces on sand particles. We also propose a new approach to update the variations of permeability and porosity for each grid block in response to both solid deformation and sand production. We show the verification of the model against analytical solutions and then apply the verified model to the simulation of sanding for a synthetic laboratory-scale problem. We present the results of our investigation on the effects of boundary stresses and fluid flow on sandstone degradation and sand production.

2. Theoretical Background

2.1. Discrete Element Method

The discrete element method is a numerical technique that explicitly models the interaction between particles instead of treating the material as a continuum medium. DEM is able to directly model grain-scale processes and capture the relative translation, sliding, and rotation between particles. It can be used to simulate problems with large deformation. A particle-based DEM analysis involves modeling a granular material using particles that usually have simple geometries, such as balls in 3D or disks in 2D.

Although DEM elements mimic individual sand particles, a DEM element does not represent one single grain. There are several differences between the DEM element and a sand grain. DEM elements are usually spherical and sand grains are not perfect spheres. DEM element surface is smooth while sand particles surfaces are much

rougher. The rougher and more angular surface has important effect during particle rotations. A DEM element is usually much larger than a sand grain in solving practical problems. Therefore, a DEM element usually represents a collection or a cluster of grains. Therefore, material parameters of a DEM element will not be the same as the intrinsic material properties of a sand grain.

We adopted the particle flow code (PFC^{3D}) developed by Itasca (Itasca, 2008) for the DEM calculations. PFC^{3D} is based on the DEM formulation proposed by Cundall and Strack (1979). In PFC^{3D}, particles are usually assumed rigid, but small overlaps are allowed at the contact points based on the stiffness of each particle. These overlaps are analogous to the deformations that occur under forces at real particle contacts of geo-materials. The contact between two neighboring particles does not exist if there is no overlapping between them.

For each time step in DEM calculations, the set of contacts is first updated from the positions of particles and walls that are entities used in PFC^{3D} to apply boundary conditions (Itasca, 2008). The force-displacement law is then applied to each contact to update the contact forces based on the relative motion between the two entities at the contact and the contact constitutive model. Next, the law of motion is applied to each particle to update its velocity and position based on the resultant force and moment arising from the contact and body forces acting on the particle. Also, the wall positions are updated based on the specified wall velocities. Contacts, which may exist between two balls or between a ball and a wall, can be formed and broken during the course of a simulation.

2.2. DEM and Fluid Flow Coupling Scheme

It is essential to perform fluid flow calculations along with solid deformation analysis in the sanding model. The seepage force due to fluid flow affects grain detachment and mobility and could mobilize disaggregated particles. On the other hand, grain motions can affect fluid flow since it changes the porosity and permeability of the material. Therefore, fluid flow and grain motions is a coupled phenomenon and should be analyzed in a coupled manner.

The formulation used in fluid flow calculations is presented here in cylindrical coordinate system since wellbore in some cases can be simplified into a 2D axisymmetrical problem. The continuity equation for fluid flow in a differential element is expressed as the difference between the entering and exiting mass being equal to accumulated mass:

$$-\frac{1}{r}\frac{\partial}{\partial r}(rv_r\rho)-\frac{1}{r}\frac{\partial}{\partial \theta}(v_\theta\rho)-\frac{\partial}{\partial z}(v_z\rho)=\frac{d}{dt}(\phi\rho) \quad [1]$$

where v_r, v_θ, v_z are the fluid velocities in the radial, tangential and vertical directions, ϕ is the porosity of rock, ρ is the density of fluid, and dt is incremental time.

From Darcy's equation (Dake, 1998), the velocity of fluid in the radial, tangential and vertical directions can be expressed as:

$$v_r=-\frac{k}{\mu}\frac{dP}{dr};\ v_\theta=-\frac{1}{r}\frac{k}{\mu}\frac{dP}{d\theta};\ v_z=-\frac{k}{\mu}\frac{dP}{dz} \quad [2]$$

where k is the rock permeability, μ is the fluid viscosity, dP/dr, $dP/d\theta$, dP/dz are the fluid pressure gradients in the radial, tangential, and vertical directions.

The compressibility of the fluid is expressed as:

$$C_f=\frac{1}{\rho}\frac{\partial\rho}{\partial p} \quad [3]$$

Combine Eqs. (1) - (3):

$$\frac{1}{r}\frac{\partial}{\partial r}\left(r\frac{k}{\mu}\frac{dP}{dr}\rho\right)+\frac{1}{r}\frac{\partial}{\partial\theta}\left(\frac{1}{r}\frac{k}{\mu}\frac{dP}{d\theta}\rho\right)+\frac{\partial}{\partial z}\left(\frac{k}{\mu}\frac{dP}{dz}\rho\right)=\rho\frac{\partial\phi}{\partial t}+\phi\frac{\partial\rho}{\partial t}=\rho\frac{\partial\phi}{\partial t}+\phi C_f\rho\frac{\partial P}{\partial t} \quad [4]$$

In Eq. (4), the term $\partial\phi/\partial t$ is obtained from DEM calculations. Fluid compressibility is assumed to be constant.

The fluid force calculation method adopted here is based on the assumption of a continuum where the size of the grid block for flow calculation is relatively large compared to the average particle diameter in the grid block. A shape function is used to interpolate pore pressures at any point inside the grid block from the calculated nodal pressures in the cylindrical coordinate system as shown in Fig. 1: . Pore pressure inside a grid block can be calculated from:

$$P(r,\,\theta) = N_i(r,\,\theta)d_e \tag{5}$$

$$N_i = [N_1 \quad N_2 \quad N_3 \quad \cdots \quad N_8];\; d_e = \begin{Bmatrix} P_1 \\ P_2 \\ \cdots\cdots \\ P_8 \end{Bmatrix} \tag{6}$$

where d_e is the nodal pressure array for the grid block, and N_i is the shape function given by Eq. (7):

$$\begin{aligned}
N_1 &= \left(1-\frac{r-r_1}{r_2-r_1}\right)\left(1-\frac{\theta-\theta_1}{\theta_2-\theta_1}\right)\left(1-\frac{z-z_1}{z_2-z_1}\right)\\
N_2 &= \left(\frac{r-r_1}{r_2-r_1}\right)\left(1-\frac{\theta-\theta_1}{\theta_2-\theta_1}\right)\left(1-\frac{z-z_1}{z_2-z_1}\right)\\
N_3 &= \left(\frac{r-r_1}{r_2-r_1}\right)\left(\frac{\theta-\theta_1}{\theta_2-\theta_1}\right)\left(1-\frac{z-z_1}{z_2-z_1}\right)\\
N_4 &= \left(1-\frac{r-r_1}{r_2-r_1}\right)\left(\frac{\theta-\theta_1}{\theta_2-\theta_1}\right)\left(1-\frac{z-z_1}{z_2-z_1}\right)\\
N_5 &= \left(1-\frac{r-r_1}{r_2-r_1}\right)\left(1-\frac{\theta-\theta_1}{\theta_2-\theta_1}\right)\left(\frac{z-z_1}{z_2-z_1}\right)\\
N_6 &= \left(\frac{r-r_1}{r_2-r_1}\right)\left(1-\frac{\theta-\theta_1}{\theta_2-\theta_1}\right)\left(\frac{z-z_1}{z_2-z_1}\right)\\
N_7 &= \left(\frac{r-r_1}{r_2-r_1}\right)\left(\frac{\theta-\theta_1}{\theta_2-\theta_1}\right)\left(\frac{z-z_1}{z_2-z_1}\right)\\
N_8 &= \left(1-\frac{r-r_1}{r_2-r_1}\right)\left(\frac{\theta-\theta_1}{\theta_2-\theta_1}\right)\left(1-\frac{z-z_1}{z_2-z_1}\right)
\end{aligned} \tag{7}$$

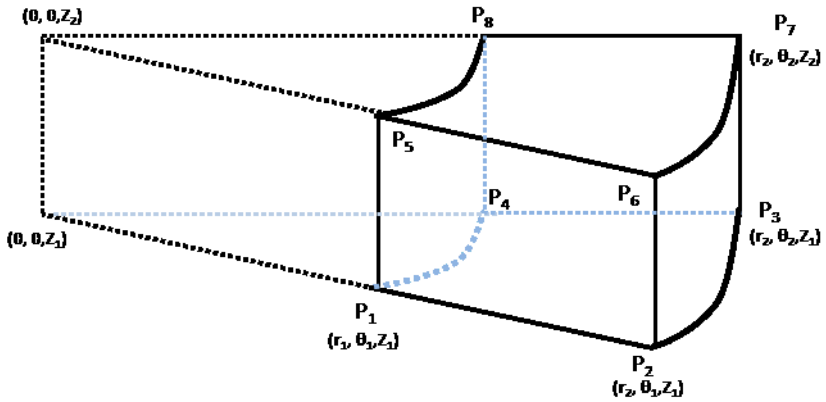

Fig. 1: A grid block for flow calculations and nodal pressures in cylindrical coordinate system

Fluid forces on the particles in the grid block are calculated by integrating the pressure over the particle surface (Fig. 2:). Consider the upper half hemisphere with known nodal pressures (P_1, P_2, P_3, P_4) as shown in Fig. 2a. The pressure at any point on the surface of the sphere with coordinate (x, y, z) can be linearly related to the four known pressures:

$$P = ax + by + cz + d = \frac{P_3 - P_4}{2r}x + \frac{P_1 - \frac{P_3+P_4}{2}}{r}y + \frac{P_2 - \frac{P_3+P_4}{2}}{r}z + \frac{P_3+P_4}{2}; \tag{8}$$

$$x = rsin\phi cos\theta, y = rsin\phi sin\theta, and\ z = rcos\phi$$

Eq. (8) can be written in the spherical coordinate system as:

$$\mathrm{P} = \frac{1}{2}[(P_3 - P_4)sin\phi cos\theta + (2P_1 - P_3 - P_4)sin\phi sin\theta + (2P_2 - P_3 - P_4)rcos\phi + (P_3 + P_4)] \quad [9]$$

The total fluid force F_y on the half hemisphere in the y direction is:

$$F_y = \int PdAsin\phi sin\theta = \int_0^{\pi}\int_0^{\frac{\pi}{2}} Pr^2(\sin\phi)^2 sin\theta d\phi d\theta = r^2\left[\frac{\pi}{3}P_1 + \frac{2}{3}P_2 + \left(\frac{\pi}{12} - \frac{1}{3}\right)(P_3 + P_4)\right] \quad [10]$$

Consider both the upper and lower hemispheres shown in Fig. 2: b; the total fluid force on a ball in the y direction is given by:

$$\begin{aligned} F_y = r^2\Big\{&\left[\frac{\pi}{3}P_1 + \frac{2}{3}P_2 + \left(\frac{\pi}{12} - \frac{1}{3}\right)(P_3 + P_4)\right] + \left[\frac{\pi}{3}P_1 + \frac{2}{3}P_6 + \left(\frac{\pi}{12} - \frac{1}{3}\right)(P_3 + P_4)\right] \\ &- \left[\frac{\pi}{3}P_5 + \frac{2}{3}P_2 + \left(\frac{\pi}{12} - \frac{1}{3}\right)(P_3 + P_4)\right] - \left[\frac{\pi}{3}P_5 + \frac{2}{3}P_6 + \left(\frac{\pi}{12} - \frac{1}{3}\right)(P_3 + P_4)\right]\Big\} \end{aligned} \quad [11]$$

After rearranging Eq. 11, we obtain:

$$F_y = \frac{2}{3}\pi r^2(P_1 - P_5) \quad [12]$$

The seepage force in the x and z directions are calculated following the same procedure used in obtaining Eq. (12).

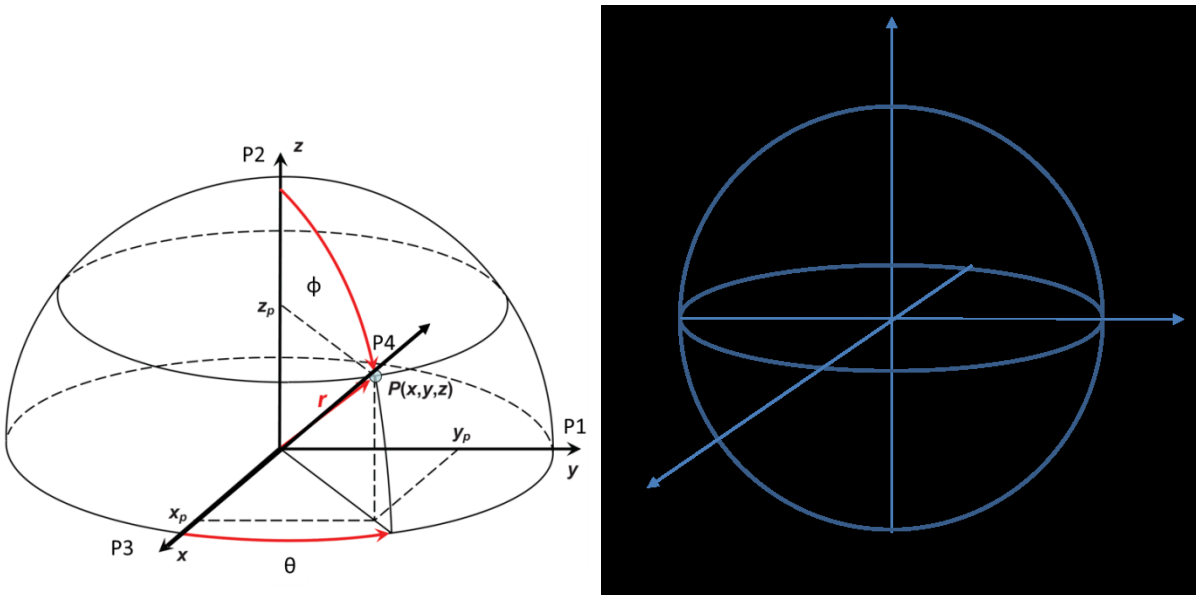

(a) Upper half hemisphere (b) Whole sphere

Fig. 2: Fluid pressure calculation on a single particle in spherical coordinate system

2.3. Scheme for Updating Permeability

A methodology was developed to assess the variations of permeability and porosity due to deformation and sand production. The stress, strain, porosity and number of particles in each grid block are determined by inserting a "measurement sphere" at the center of the grid block. The measurement sphere is a built-in tool in PFC^{3D} to help user to calculate quantities such as porosity, stress and strain rate in a specific measurement volume (Itasca, 2008).

To update permeability, the number of particles with centroids that lie in the specific measurement sphere is determined in the beginning and end of each time step to track particle movements. If the number of particles in the beginning is found to be equal to or smaller than the number of particles at the end of the time step, no sanding is assumed to have taken place from that volume. In this case, the permeability is updated based on volumetric strain using the modified version of the Kozeny-Carman's equation (Tortike, 1991):

$$k_1 = k_0 \frac{\left(1 + \frac{\varepsilon_v}{\phi_0}\right)^3}{1 + \varepsilon_v} \quad [13]$$

where k_0 is the initial permeability in the grid block, ϕ_0 is the initial porosity, ε_v is the volumetric strain calculated from the volumetric strain rate in the measurement sphere:

$$\varepsilon_v = \sum \dot{\varepsilon}_v \Delta t \quad [14]$$

where $\dot{\varepsilon}_v$ is the instantaneous strain rate determined from the velocities of all particles within the measurement sphere at the end of each DEM time step, and Δt is the DEM time step (Itasca, 2008):

$$\Delta t = \sqrt{\frac{m}{K}} \quad [15]$$

where m is the mass of the particle and K is the stiffness of the particle. The calculated DEM time step in our analysis ranged from 1×10^{-7} to 1×10^{-6} seconds.

If the number of particles in the beginning is found to be larger than the number of particles at the end of the time step, denoted here as N, the element permeability is updated based on the updated porosity of the element. If the porosity measured in this block is smaller than a certain threshold, denoted here as ϕ, the permeability is updated by interpolating between the original permeability and an upper-bound permeability. The upper-bound permeability was chosen to be 100 Darcies after a sensitivity work which will be presented in Section 4.2.

$$k_{update} = k_0 + (100 - k_0)\frac{\phi_1 - \phi_{full}}{T - \phi_{full}}$$
$$n_{update} = n_0 + (0.95 - n_0)\frac{\phi_1 - \phi_{full}}{T - \phi_{full}} \quad [16]$$

where ϕ_{full} is the porosity measured from the measurement sphere before the onset of sanding from the block, ϕ_1 is the porosity measured from measurement sphere at the end of the iteration, k_0 is the permeability at the beginning of the iterations. In this work, the porosity of the fully sanded block T was assumed to be 0.85.

If the porosity exceeds 0.85, the grid block is assumed to have completed sand production. In this case, the permeability is assigned a high value (in this study, 100 Darcy). The procedure used for updating the porosity and permeability is presented in Fig. 3.

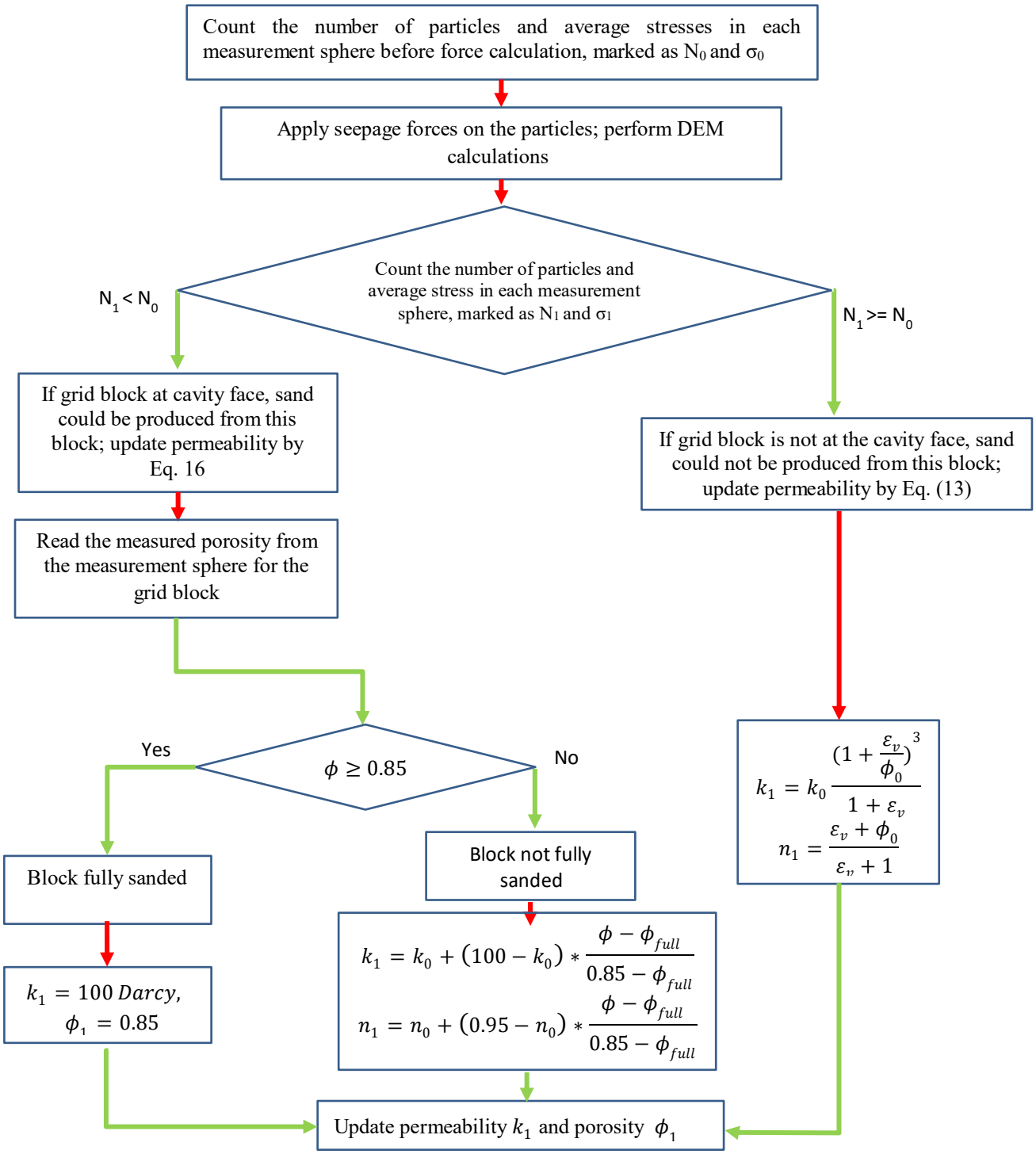

Fig. 3: The scheme for updating permeability and porosity

3. Model Verification

The coupled DEM-flow model described here was verified against the results of analytical solutions proposed by Risnes et al. (1982). Details of the verification process are discussed below.

3.1. Analytical Solution

Risnes et al. (1982) derived analytical expressions for stress distribution around a borehole assuming axial symmetry and plane strain conditions using the Mohr-Coulomb failure criterion. Fig. 4 shows the model geometry used by Risnes et al. (1982).

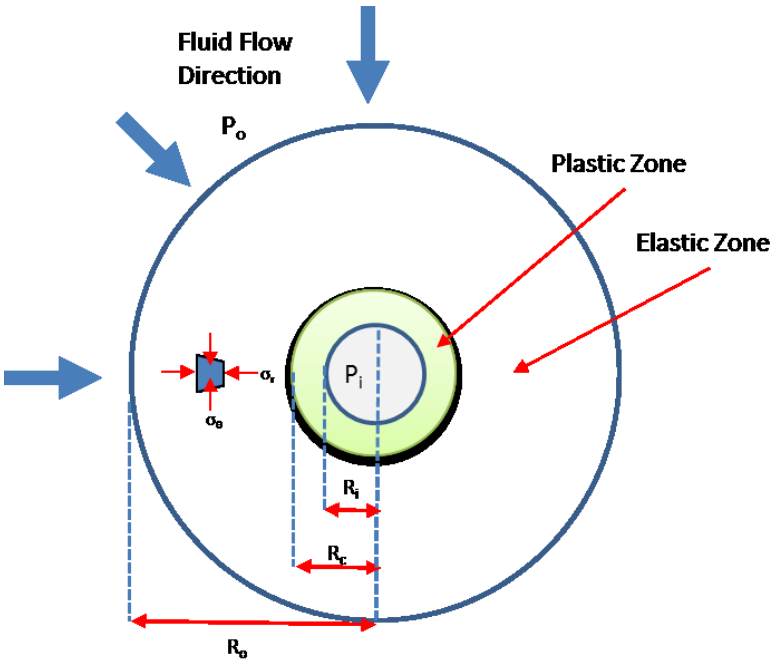

Fig. 4: Model geometry considered by Risnes et al. (1982)

The expressions for the stresses in both the plastic and elastic zones are given in Eqs. (17) through (21). Within the plastic zone, the radial and tangential total stress, σ_r and σ_θ, at a radial distance of r can be determined from Risnes et al. (1982):

$$\sigma_r = P_i + \frac{\mu q}{2\pi h k_c}\ln\frac{r}{R_i} + \frac{1}{\gamma}\left(2c\tan\alpha - \frac{\mu q}{2\pi h k_c}\right)\left[\left(\frac{r}{R_i}\right)^{\gamma} - 1\right] \quad [17]$$

$$\sigma_\theta = P_i + \frac{\mu q}{2\pi h k_c}\left(1 + \ln\frac{r}{R_i}\right) + \frac{1}{\gamma}\left(2c\tan\alpha - \frac{\mu q}{2\pi h k_c}\right)\left[(\gamma+1)\left(\frac{r}{R_i}\right)^{\gamma} - 1\right] \quad [18]$$

where P_i and P_0 are the fluid pressures at the inner and outer cylindrical boundaries, c is the cohesion of the material, α is the failure angle which is equal to $\pi/4 + \phi/2$, ϕ is the internal friction angle, $\gamma = \tan^2\alpha - 1$, μ is the fluid viscosity, k_c is the permeability of the material in the plastic zone, and q is the fluid flow rate calculated from:

$$q = \frac{2\pi k h(P_0 - P_i)}{\mu \ln\left(\frac{R_0}{R_i}\right)} \quad [19]$$

where h is the height of the model.

Radial and tangential total stresses in the elastic zone are calculated from Risnes et al. (1982):

$$\sigma_r = \sigma_{r0} + (\sigma_{r0} - \sigma_{rc})\frac{R_c^2}{R_0^2 - R_c^2}\left[1 - \left(\frac{R_0}{r}\right)^2\right] - (P_0 - P_c)\frac{1-2\upsilon}{2(1-\upsilon)}\beta\left\{\frac{R_c^2}{R_0^2 - R_c^2}\left[1 - \left(\frac{R_0}{r}\right)^2\right] + \frac{\ln\frac{R_0}{r}}{\ln\frac{R_0}{R_c}}\right\} \quad [20]$$

$$\sigma_\theta = \sigma_{r0} + (\sigma_{r0} - \sigma_{rc})\frac{R_c^2}{R_0^2 - R_c^2}\left[1 + \left(\frac{R_0}{r}\right)^2\right] - (P_0 - P_c)\frac{1-2\upsilon}{2(1-\upsilon)}\beta\left\{\frac{R_c^2}{R_0^2 - R_c^2}\left[1 + \left(\frac{R_0}{r}\right)^2\right] + \frac{\ln\frac{R_0}{r} - 1}{\ln\frac{R_0}{R_c}}\right\} \quad [21]$$

where σ_{ro} is the radial stress at the outer boundary, σ_{rc} and P_c are the radial total stress and the fluid pressure at the plastic-elastic boundary ($r = R_c$), υ is the material Poisson's ratio and β is the coefficient of rock compressibility which is equal to $1 - C_r/C_b$, C_r is the rock matrix compressibility, and C_b is the rock bulk compressibility.

3.2. Input Parameters

We used Castlegate sandstone properties in the analytical and numerical models for a Thick-Walled Cylindrical (TWC) sample with the inner and outer radius of 8 mm and 80 mm, respectively, with a sample height of 15 mm. Castlegate sandstone is a weak, high-porosity sandstone with low clay content, which has been used in triaxial testing (e.g., Bradford and cook, 1994). Rahmati et al. (2013b) calibrated the microproperties of Castlegate sandstone and performed DEM simulation of Thick Walled Cylinder samples to study borehole breakout mechanisms (Rahmati et al., 2013c). The unconfined compressive strength is around 20 MPa, the porosity is 0.25 and the permeability is 500 to 1000 mD (Rahmati et al., 2013b). Cheung (2010) reported that the cement content for the Castlegate sandstones is equal to 6.4% by mass. Rahmati et al. (2013b) calibrated the macro properties of Castigate sandstone from laboratory triaxial tests. Cohesion, friction angle, and elastic properties were determined from triaxial tests on Castlegate sandstone. Young's modulus was based on a value calculated at 50% of the peak stress as recommended by Schanz et al. (1999). Poisson's ratio was averaged at different effective confining stresses. The macro parameters for the numerical model are summarized in Table 1.

Table 1. Analytical input data for flow analysis and Castlegate sandstone properties

Sample Dimension and Fluid Properties		Rock Properties (Rahmati, 2013)	
Outer boundary pressure **Po** (MPa)	Variable	Possion's ratio **ν**	0.2
Inner boundary pressure **Pi** (MPa)	0	$\boldsymbol{\beta = 1 - C_r / C_b}$	1
Sample thickness **h** (cm)	1.5	Cohesion **C** (MPa)	4.3
Sample inner radius **Ri** (cm)	0.8	Friction Angle $\boldsymbol{\phi}$ (deg)	46.5
Sample Outer radius **Ro** (cm)	8	$\alpha = \frac{\pi}{4} + \frac{\phi}{2}$ (deg)	61.5
Water viscosity **μ** (cp)	1	Elastic zone permeability $\mathbf{K_e}$ (Darcy)	0.6
Fluid flow rate **q** (cm^3/s)	By case	Plastic zone permeability $\mathbf{K_c}$ (Darcy)	0.6

The DEM model was generated using two horizontal and one cylindrical rigid wall with a radius of 80 mm and height of 15 mm (Fig. 5). Table 2 presents the micro-parameters of DEM particles calibrated using triaxial test results (Rahmati, 2013). A constant radial stress of 60 MPa was applied at the outer boundary by moving the outer cylindrical wall using a servo control algorithm while the top and the base platens were fixed in all directions. An inner hole of 8 mm radius was then drilled by removing particles. An initial calculation was carried out to eliminate unbalanced forces at the contact. The calculation continued until the ratio of average unbalanced force to the average contact forces converged to a value of less than 1%.

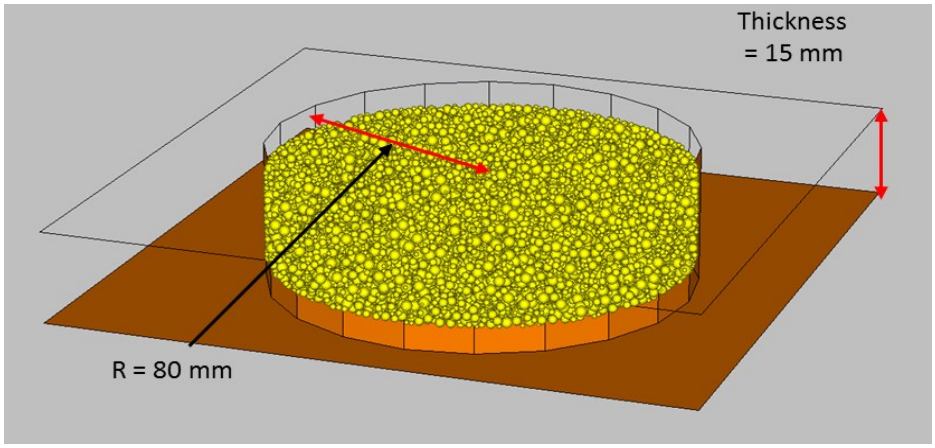

Fig. 5: DEM model for the TWC test

Table 2: Micro properties of Castlegate sandstone for DEM simulations (Rahmati, 2013)

Particle properties		Parallel bond properties	
Yong's modulus E (GPa)	7	Yong's modulus E_{pb} (GPa)	20
K_S/K_N	0.2	$(K_S/K_N)_{pb}$	0.2
Partial friction coefficient μ	1.5	$S_{N\ pb}$ (MPa)	400
Particle radius R_p (mm)	0.4 to 1.3	$S_{S\ pb}$ (MPa)	900
Particle density (kg/m^3)	2,650	Degree of bonding λ	0.3

The fluid model was introduced by dividing the domain into 324 flow elements with 9 sections in the radial direction, 18 sections in the circumferential direction, and 2 in the vertical direction. Fig. 6 shows the sample geometry and the flow mesh.

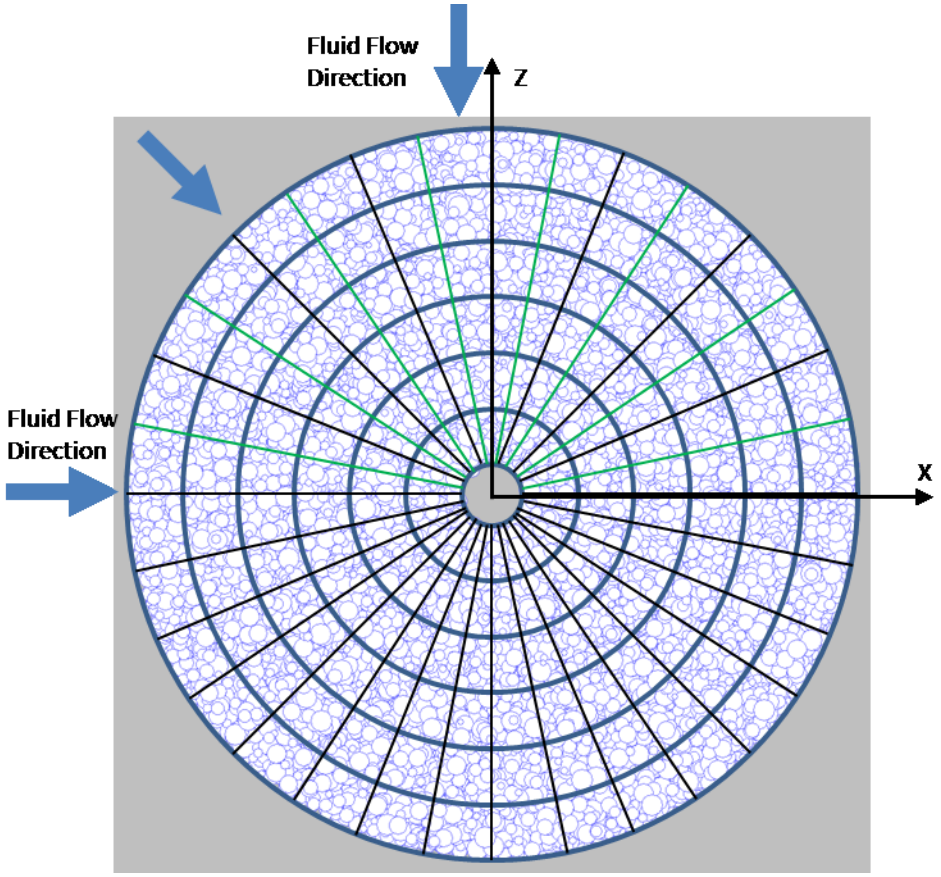

(a) Top plan view (x-z plan)

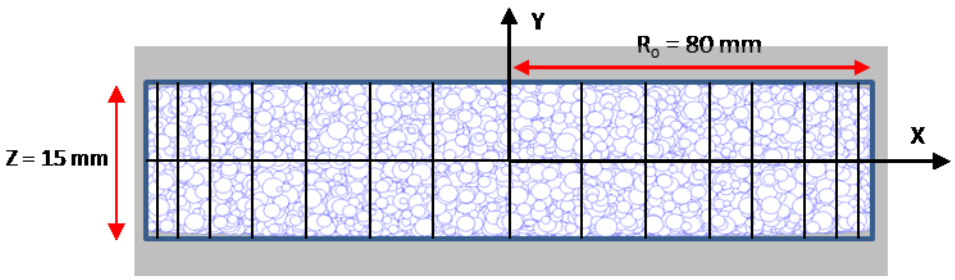

(b) Side plan view (x-y plan)

Fig. 6: DEM model of the TWC test overlain by grid blocks for flow analysis in cylindrical coordinate system

Water was injected from the outer cylindrical boundary into the specimen using the flow boundary conditions shown in Table 1. Since sanding is not considered in the analytical model, the fluid pressure at the outer boundary was kept below a critical level to avoid any sand mobilization toward the center hole. Nodal pressures in the flow model were transferred to the DEM model where the pressures were converted to seepage forces and applied on each particle. The DEM calculations were then performed until the solutions converged within a small tolerance.

3.3 Verification Results of the Analysis

The radial and tangential stresses in the specimens were determined by calculating the average stress in the measurement spheres. Comparisons of the numerical and analytical results for tangential and radial stress along the radial direction are shown in Fig. 7 and 8.

The width of the plastic zone can be considered to extend from the face of the borehole to the location of maximum tangential stress. Fig. 7 shows the radial and tangential stress profiles at a confining stress of 60 MPa without fluid flow. It is observed that a plastic zone has already been developed around the hole even when there is no fluid flow. However, with fluid flow, the plastic zone further expands in both the numerical and analytical models (Fig. 8). The tangential and radial stresses of both analytical and numerical solutions approach the boundary stress of 60 MPa at the outer boundary. The difference between the peak values for the analytical and numerical tangential stresses can partly be attributed to the averaging procedure in calculating stresses in the numerical model which has a smoothing effect on the stress calculations (Climent et al., 2014).

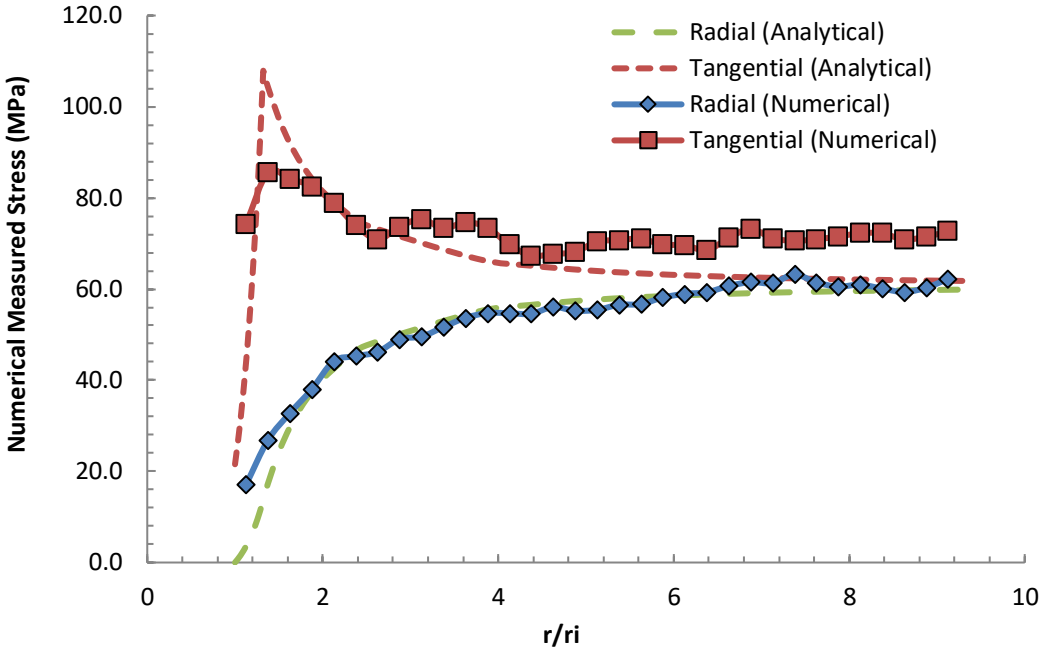

Fig. 7: Comparison between numerical and analytical results for tangential and radial stress in the radial direction for the case without fluid flow

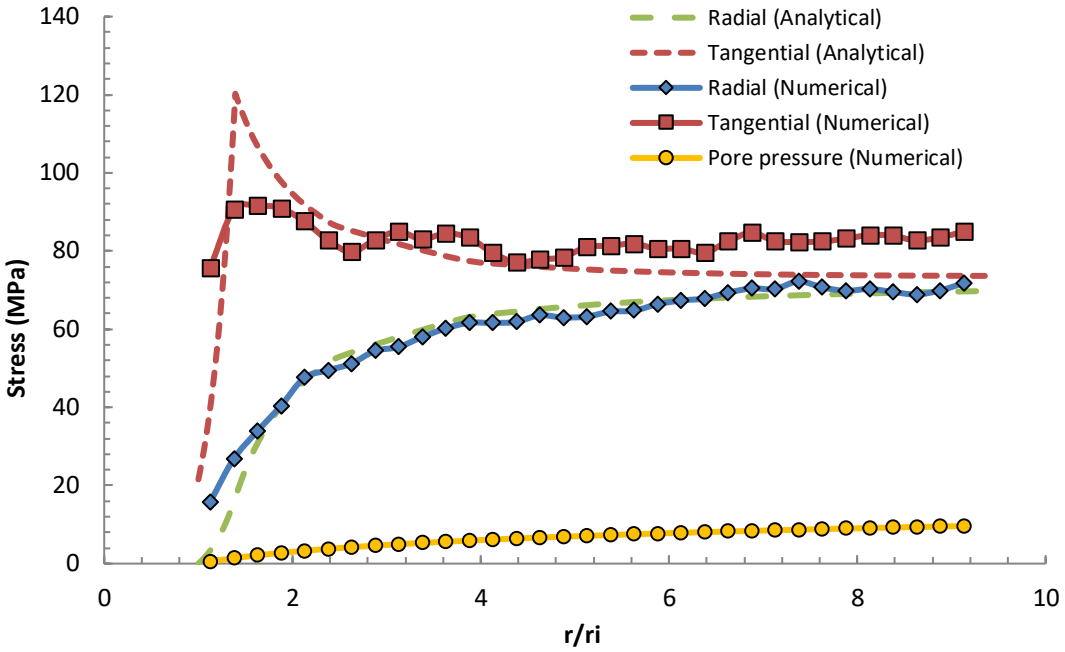

Fig. 8: Comparison between numerical and analytical results for total tangential and radial stress in the radial direction for the case with fluid flow and 10 MPa for outer boundary fluid pressure

4. Sand Production Simulation

In this section, we describe the simulation of a synthetic sanding test using the DEM model. We first specify the model geometry and boundary conditions. Next, we describe the results of a series of sensitivity analysis to optimize the number of DEM steps that need to be performed within each numerical iteration.

4.1 Model Geometry and Boundary Conditions

The DEM model was generated in a rectangular box with length, width and depth equal to 120 mm, 120mm, and 15 mm, respectively. The domain is bounded by six frictionless rigid walls (Fig. 9). The model creation procedure followed the same way as in the verification model. Parallel bonds were randomly imposed on 30% of the contacts after the material generation stage. The bond radius multiplier was varied randomly between 0 and 1 (Rahmati, 2013b), based on the observations from Scanning Electron Microscope (SEM) images of Castlegate sandstone (Cheung, 2010). Based on the SEM image of Castlegate sandstone in Fig. 10, it is evident that not every grain-grain contact in the Castelgate sandstone is cemented. Contact A is a cemented, Contact B is not cemented, and contact C has broken cementation. Meanwhile, the degree of cementation varies at the contacts. Table 2 presents the DEM micro-properties for this model.

DEM simulations started with the sample compaction by applying three perpendicular and unequal stresses using a servo control algorithm (Itasca, 2008). The vertical borehole with 8 mm radius was drilled by gradually decreasing the grain stiffness inside the borehole to zero followed by removing the grains inside the borehole. Initial analysis was carried out until the average unbalanced forces divided by the average contact forces was smaller than 1%.

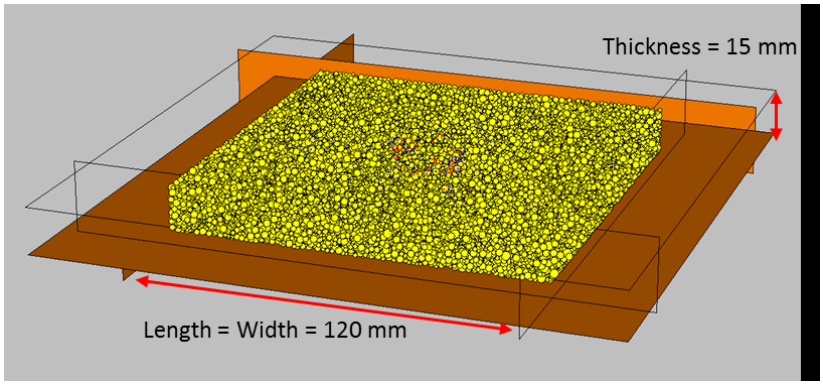

Fig. 9: DEM sanding model

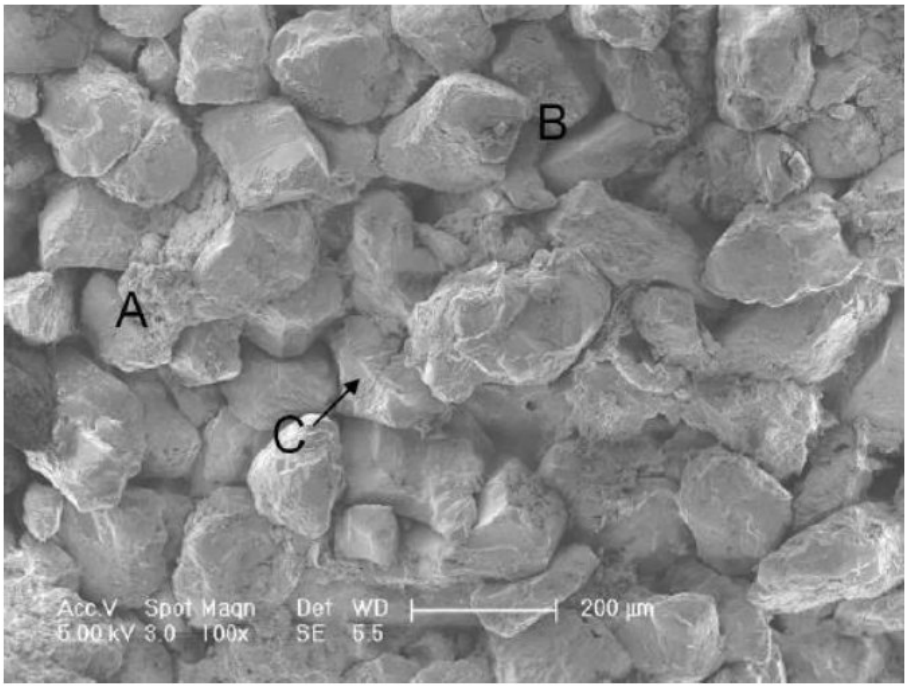

Fig. 10: The SEM image for the Castlegate sandstone (Cheung, 2010)

The fluid flow model was linked to the DEM model. The flow model has 324 grid blocks with nine sections in the radial direction, 18 sections in circumferential directions, and two in the vertical direction, as shown in Fig. 11.

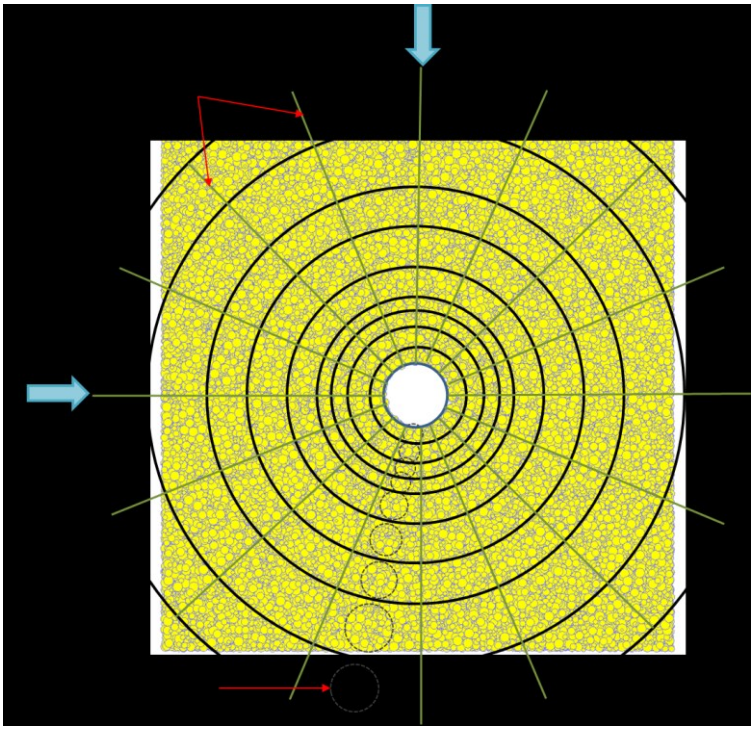

Fig. 11: Block sample overlain by grid blocks in cylindrical coordinate system

In linking fluid flow-DEM calculations, convergence was considered to be achieved when the number of particles in the measurement spheres, as well as permeability and porosity in each grid block, had converged to a tolerance of 5%.

4.2. Sensitivity Analysis for Model Optimization

In order to determine the effects of various parameters in the model, a sensitivity study was performed to optimize the size of the measurement sphere, the permeability of the sanding zone used in Eq. (16), and also the number of DEM steps required in each numerical iteration. A uniform far field effective stress of 60 MPa was applied which was enough to induce breakage of bonds near the hole before the application of fluid flow. An outer boundary fluid pressure of 0.5 MPa was applied resulting in the flow rate of 11.53 cm^3/sec in wellbore surface.

The sanding response was studied for different DEM steps in each DEM-fluid flow iteration. Fig. 12 shows the effects on sanding due to the number of DEM steps. The solutions seemingly are converging at about 10,000 DEM steps. However, the total produced sand mass for different number of DEM steps was the same. Therefore, we chose 10,000 DEM steps for each iteration in all subsequent analyses.

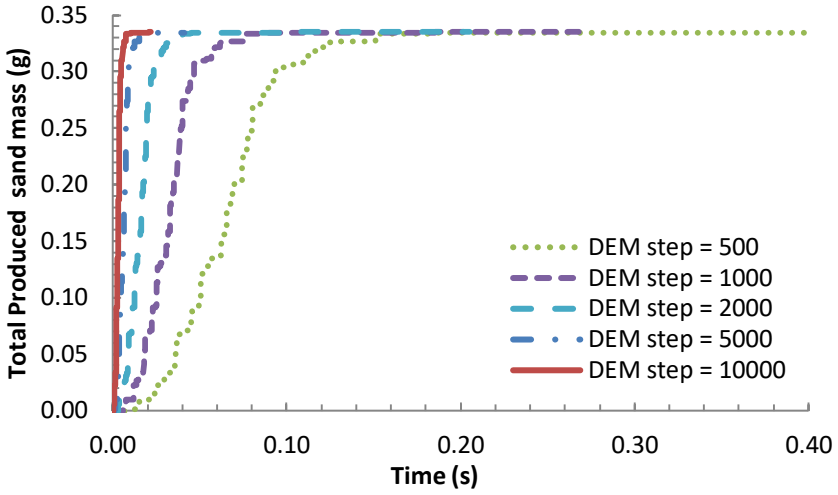

Fig. 12: Produced sand mass for different number of DEM steps in each DEM-fluid flow iteration

A sensitivity analysis was performed to study the effect of the assigned permeability for the sanded zone in Eq. (16). A fluid pressure of 0.1 MPa was applied at the outer boundary with an in situ effective stress of 60 MPa. The permeability assigned to the fully produced cell was fixed during each test. Fig. 13 shows that the sanding response is not sensitive to the permeability of the produced zone for k values greater than 50 Darcy. Therefore, we assigned a permeability of 100 Darcy in all subsequent analyses.

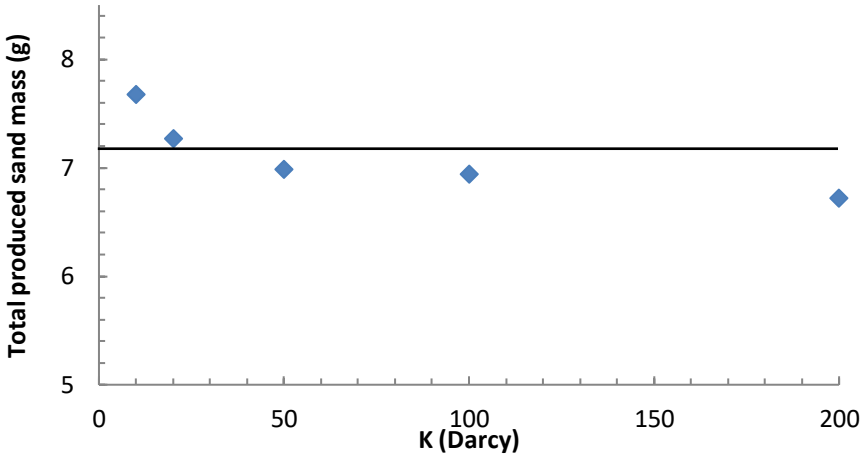

Fig. 13: Cumulative sanding for different values of permeability for the produced zone

Another study was performed to study the effect of the size of the measurement sphere on the results. Significant errors in the calculated stress, strain, and porosity result when the measurement sphere includes only four or less particles (Itasca, 2008). On the other hand, inaccurate permeability calculations result when large measurement sphere sizes that cover more than one flow grid block are selected. We chose the size of the grid

block in such a way to include a minimum six particles. The final size of the measurement sphere was chosen to be 1.6 times the length of the grid block, so that it would circumscribe the flow grid blocks and include a representative number of particles in the sphere.

4.3 Effect of Maximum and Minimum Horizontal Effective Stresses and Pore Pressure on Rock Degradation and Sanding

In this section we study the effect of boundary effective stress and pressure on sandstone degradation and sanding. Two cases were considered: (1) the horizontal effective stresses were equal to 60 MPa, (2) maximum and minimum horizontal stresses were equal to 60 and 30 MPa, respectively. In both cases, the fluid pressure at the outer boundary was kept constant at 10 MPa. The DEM – fluid flow analysis was cycled until 0.03 sec.

A map of broken bonds of a horizontal section are shown in **Error! Reference source not found.** for different boundary stress and pressure cases after 0.12 sec. Micro-failure at the contacts is represented by red and blue for bonds failed in tension and shear, respectively. **Error! Reference source not found.**a shows uniform breakout for the case with uniform boundary stress without fluid flow. **Error! Reference source not found.**b shows V-shaped breakout for the same case but with uneven boundary stresses. Some sand particles are observed to be produced from the breakout zone by seepage forces after the application of fluid flow.

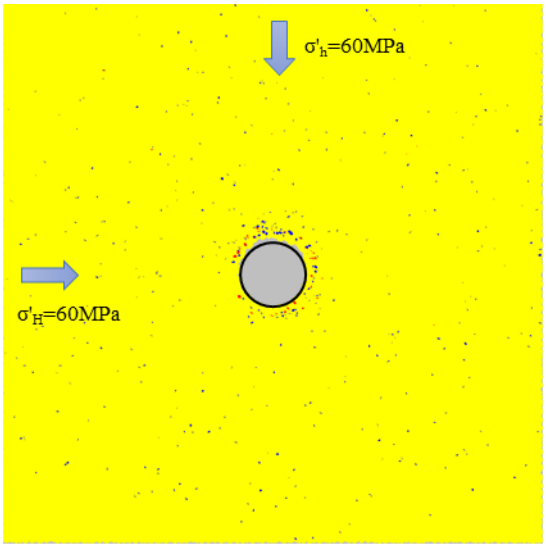

(a)

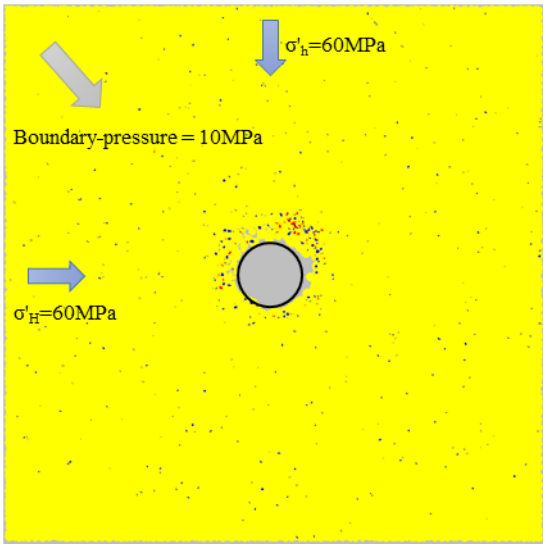

(b)

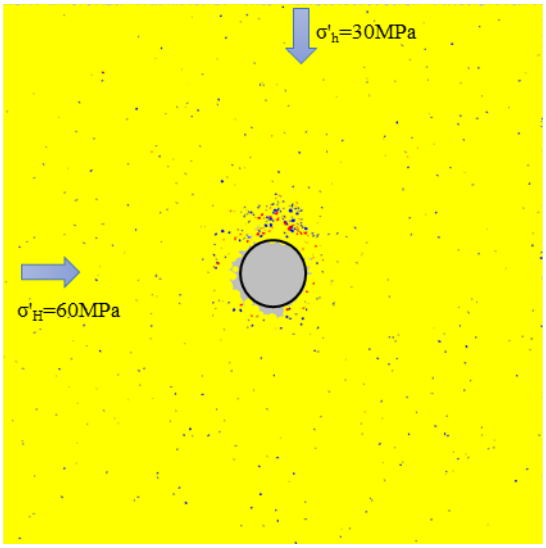

(c)

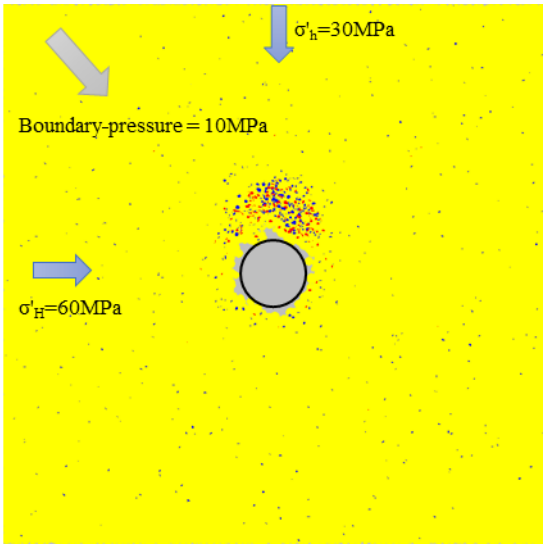

(d)

Figure 14: Cross section of borehole breakout and sanding zone for different far-field stress. (a) isotropic far field stress case, before the application of fluid flow, (b) after the application of fluid flow with pore pressure = 10 MPa, at time **= 0.03 sec, (c) anisotropic far field stress case, before the application of fluid flow,** (d) after the application of fluid flow with pore pressure = 10 MPa, at time = 0.03 sec.

Fig. 16 compares the maximum thickness of the plastic zone for the dry case based on the DEM solutions (Fig. 14a and c) and the analytical solutions in dash line. The analytical formulation of isotropic case is presented by Risnes et al (1982), and the analytical formulation of anisotropic case is presented by Fjar (2008). The macro properties of Castlegate sandstone used in analytical solution is listed in Table 1. For 60 MPa isotropic effective stress case, analytical solutions result in 2.6 mm for the maximum thickness of the plastic zone while DEM measurement from Fig. 14a indicate 3 mm for the maximum plastic thickness in average. For the case with σ'_h= 30 MPa, DEM and analytical solution result in 8 mm and 7 mm for the thickness of the plastic zone, respectively. Results indicate a reasonable agreement between the DEM and analytical solutions before introducing the fluid flow. Based on Fig. 14, the plastic zone further expands once the pressure drawdown is applied.

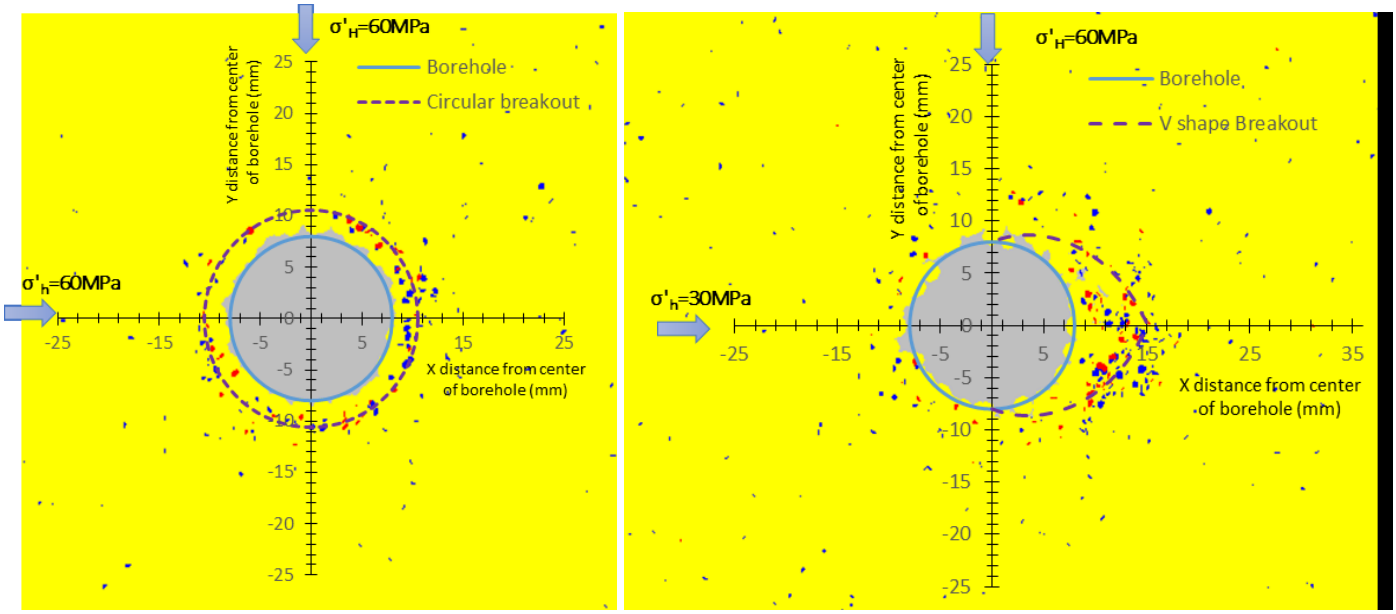

(a) (b)

Fig. 15: The analytical solution of plastic zone for the dry case of (a) isotropic boundary effective stress (b) anisotropic boundary effective stress.

Fig. 166 shows the effect of the minor principle stress on the produced sand. As expected, larger amount of sand is produced for the case with anisotropic boundary effective stress than the isotropic counterpart. However, sanding is observed to be only slightly different for the vastly different minimum far field effective stresses.

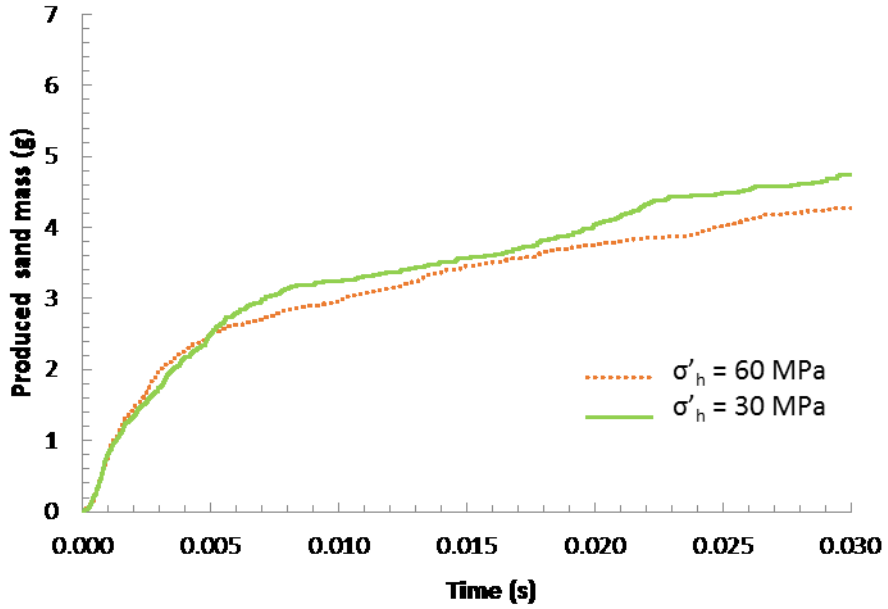

Fig. 16: Cumulative sanding for different far-field stress conditions

Next, both boundary effective stresses were kept constant at 50 MPa in a series of analysis with varying outer boundary fluid pressure from 0.1 MPa to 15 MPa. 7 shows the high-rate sanding at the beginning of the simulation leading to stabilized sanding at different times. The total amount of sand produced and steady-state time increase significantly for outer boundary pressures larger than 10 MPa. We notice a significant jump in the amount of produced sand when the boundary pressure increases from 10 to 15 MPa. The reason is mainly due to the contribution of the seepage forces in additional sandstone degradation through more and faster removal of degraded materials.

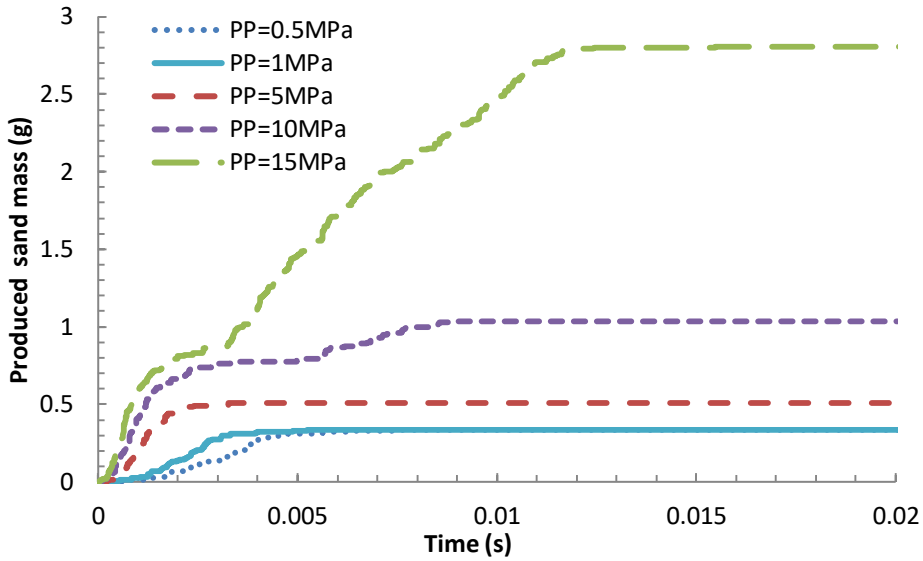

Fig. 17: Sand production for different boundary pressures

4.4 Simulation of Step-Rate Sanding Tests

We simulated a synthetic sanding test on a hollow cylinder sample using the model presented in Fig. 9 and Fig. 11 and Table 2. In the simulations, the outer boundary effective stress was incrementally increased with the step-rate increase of the fluid pressure within each boundary stress increment (Fig. 18). The analysis for each step continued until the steady-state condition was reached (sanding rate is equal to zero at this stage). Fig. 18 indicates the onset of sanding at the outer boundary effective stress of 30 MPa. Cumulative sand production

shows a gradual increase for each increase in the boundary effective stress or pressure. However, sanding stabilizes within each increment. Massive sanding occurs when the boundary effective stress and pressure reach 58 and 20 MPa, respectively.

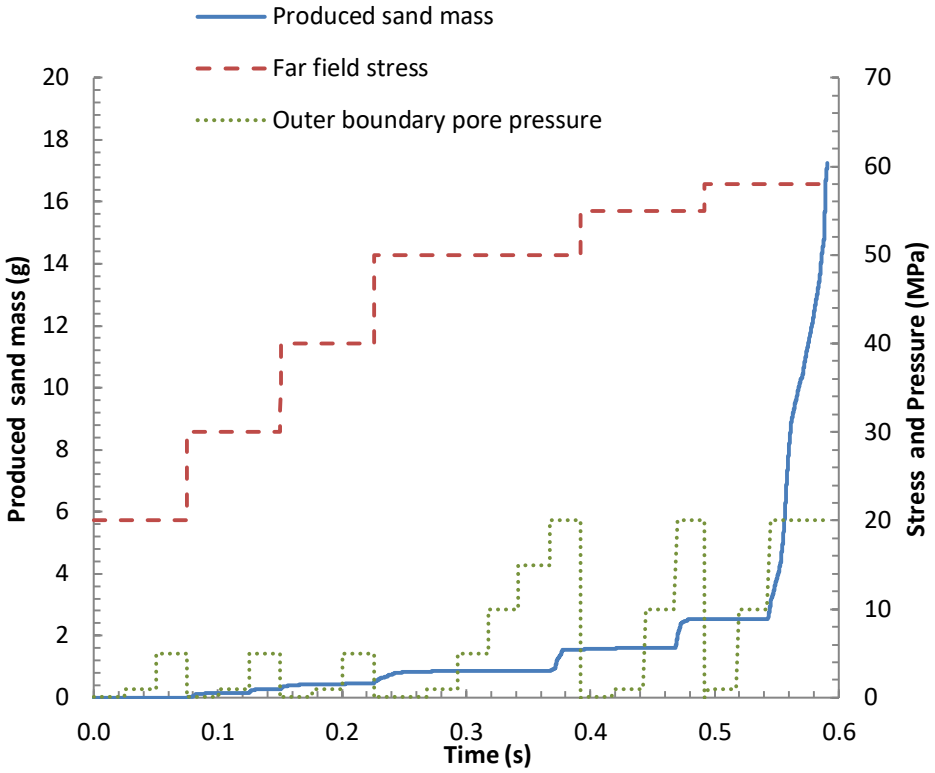

Fig. 18: Sanding response under incrementally increasing boundary stress and pressure for final boundary stress of 58 MPa

To further examine the role of fluid flow, we repeated the same analysis but changed the final modelling step (Fig. 19). The last loading step in Fig. 19 shows the boundary effective stress equal to 65 MPa with lower boundary pressure of 1 MPa. Despite significantly higher boundary effective stress, we can see much less sanding compared to the last step in Fig. 18. The large boundary pressures in Fig. 18 result in larger seepage forces leading to further removal of detached sand particles, redistribution of contact forces, and propagation of the degraded zone.

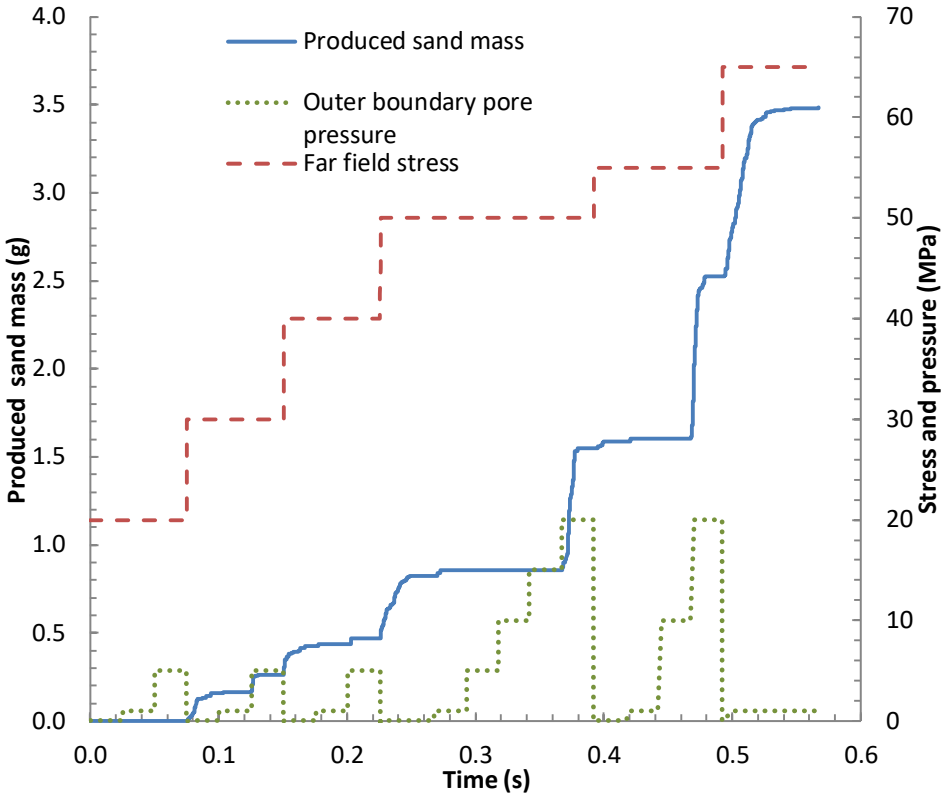

Fig. 19: Sanding response under incrementally increasing boundary stress and pressure for final boundary stress of 65 MPa

Fig. 20a shows little degradation at a boundary effective stress of 50 MPa and boundary pressure of 20 MPa. Fig. 20b shows a larger size of the degraded zone at the boundary stress of 58 MPa and boundary pressure of 20 MPa. The degraded zone is significantly smaller at the higher boundary stress of 65 MPa and low boundary pressure of 1 MPa (Fig. 20c). However, the degraded zone is significantly enlarged when the outer boundary pore pressure reaches 20 MPa. The reason for the above observation is that the additional degradation is due to seepage forces being strong enough to remove more particles leading to stress redistribution thus more degradation is observed. . When the outer boundary pore pressure is small, say 1 MPa, the fluid force near the wellbore face is not large enough to break the bond between the particles. The case with 65 MPa's confining stress shows a higher tangential stress resulting in higher frictional resistance, thus, less sand production at the same levels of boundary pressure. This may explain lower sand production for the case with 65 MPa confining stress in the period between 0.52 to 0.6 s.

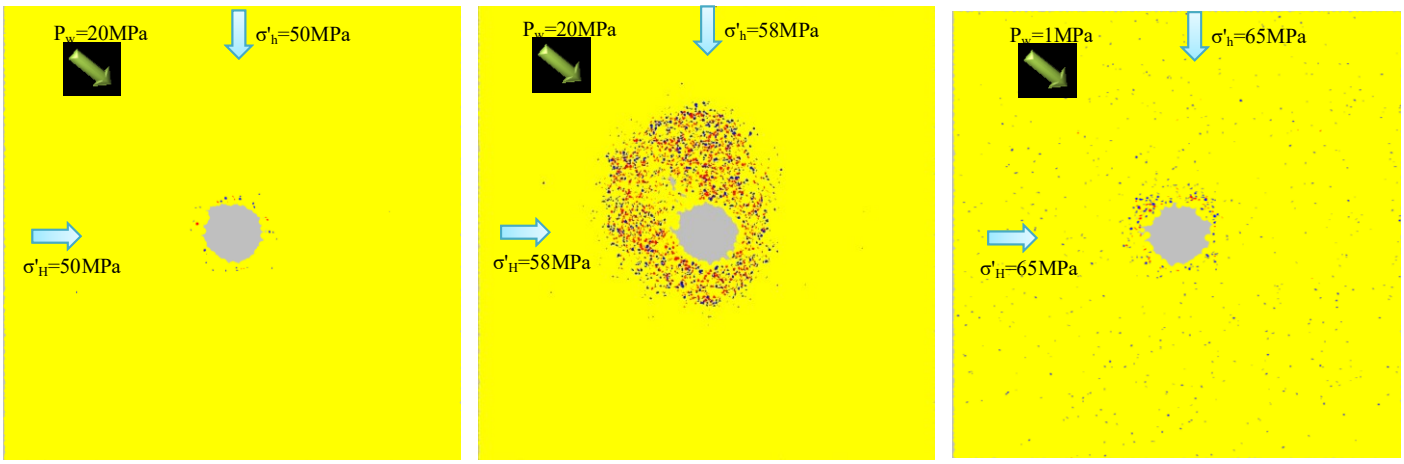

(a) (b) (c)

Fig. 20: Cross section of failure shape around wellbore. (a) Far field effective stress = 50 MPa, outer boundary pressure = 20 MPa. (b) Far field effective stress = 58 MPa, outer boundary pressure = 20 MPa. (c) Far field effective stress = 65 MPa, Outer boundary pressure = 1 MPa

5. Conclusions

A sand production model has been presented by coupling DEM model with a fluid flow model. The model has been checked with analytical solutions and applied to examine sanding process in synthetic sanding tests. The model accounts for permeability and porosity changes due to solid deformation and sand production. Some simulation results are summarized below:

1. A circular breakout was found for the case of isotropic boundary stress with $\sigma_H = \sigma_h = 60$MPa. The breakout morphology changes to V-shaped breakout with unequal boundary stresses when σ_H=60 MPa and σ_h = 30MPa .

2. Larger sanding occurs with with unequal boundary stresses when σ_H=60 MPa and σ_h = 30 MPa, compared to the case with isotropic boundary stress with $\sigma_H = \sigma_h = 60$MPa.

3. Sand production occurs from degraded zones where most bond failures has occurred. Sand production from V-shaped breakout changes the wellbore shape from circle to ellipse.

4. The boundary stress plays a major role in sand production through sandstone degradation. However, less sanding occurs at higher boundary effective stress but considerably lower boundary pressure due to ineffective removal of the degraded materials for weaker seepage forces. For high boundary pressure, seepage force plays a major role in sand production as it removes degraded materials, results in stress redistribution which can then contribute to further degradation and sanding. More sand production occurs at lower far-field stress (in this case, 58 MPa) but higher boundary pressure (in this case, 20 MPa).

Acknowledgements

The authors would like to acknowledge the research funding for this study provided by NSERC through their Discovery Grants Program.

References

Boutt, D. F., Cook, B. K., Williams, J. R., 2011. A coupled fluid-solid model for problems in geomechanics: Application to sand production. *Int. J. Numer. Anal. Met*. 35, 997-1018.

Bradford, I. D. R., Cook, J. M., 1994. A semi-analytical elastoplastic model for wellbore stability with applications to sanding. *In. Proc. Eurck*. Rotterdam. 347-351.

Chan, D., 1993. Numerical Simulation of Wet Granular Flow, *International Conference on Soft Soil Engineering*, Guangzhou, China. 68-73.

Chan, D., Tipthavonnukul, S., 2008. Numerical simulation of Granular Particles Movement in Fluid Flow. *Int. J. Nonlinear Sci.* 9(3), 229-248.

Cheung, L. Y. G., 2010. Micromechanics of Sand Production in oil wells. (PhD Thesis). University of London, United Kingdom.

Climent, N., Arroyo, M., O'Sullivan, C., and Gens, A., 2014. Sand production simulation coupling DEM with CFD. *Eur. J. Environ. Civ. En.* 18(9), 983-1008.

Cook, B. K., Noble, D. R., and Williams, J. R., 2004. A direct simulation method for particle-fluid systems. *Eng. Computation*. 21, 151-168.

Cundall, P. A., and Strack, O. D. L., 1979. A discrete numerical model for granular assemblies. *Géotechnique*, 29(1), 47-65.

Dake, L. P., 1998. Fundamentals of Reservoir Engineering, seventeenth ed. Elsevier, Amsterdam.

Detournay, C., and Wu, B., 2006. Semi-analytical models for predicting the amount and rate of sand production. *EUROCK 2006: Multiphysics coupling and Long Term Behavior in Rock Mechanics*. Taylor & Francis. 373-380.

Fjær, E., Holt, R. M., Horsrud, P., Raaen, A. M., and Risnes, R., 2008. Petroleum Related Rock Mechanics, second ed. Boulevard, Langford Lane, Kidlington, Oxford, UK. 341-366.

Grof, Z., Cook, J., Lawrence, C. J., and Stepanek, F., 2009. The interaction between small clusters of cohesive particles and laminar flow: Coupled DEM/CFD approach. *J. Petrol. Sci. Eng.* 66, 24-32.

Itasca Consulting Group., 2008. PFC3D version 4.0 Manual. Minneapolis.

Li, P., Chalaturnyk, R. J., 2006. Permeability Variations Associated with Shearing and Isotropic Unlading During the SAGD Process. *J. Can. Petrol. Technol.* 45(1), 54-61.

Potyondy, D. O., Cundall, P. A., 2004. A bonded particle model for rock. *Int. J. Rock. Mech. Min.* 41(8), 1329-1364.

Quadros, R., Vargas, E.A., Goncalves, C.J., Prestes, A., 2010. Analysis of sand production processes at the pore scale using the discrete element method and lattice Bolzman procedures. *Proceedings of the 44th US Rock Mechanics Symposium and 5th U.S. – Canada Rock Mechanics Symposium*. Salt Lake City, UT. USA.

Rahmati, H., Jafarpour, M., Azadbakht, S., Nouri, A., Vaziri, H., Chan, D., Xiao, Y., 2013. Review of Sand production Prediction Models. *J. Petrol. Eng.* 2013, 1-16.

Rahmati, H., Nouri, A., Chan, D., Vaziri, H., 2013b. Simulation of Drilling-Induced Compaction Bands Using Discrete Element Method, *Int. J. Numer. Anal. Met*. 38(1), 37-50.

Rahmati, H., Nouri, A., Chan, D., Xiao, Y., 2013c. Systematic Calibration Procedure for DEM Parallel-bond Models, *Canadian Energy Technology & Innovation*. 1(4).

Risnes, R., Bratli, R. K., and Horsrud, P., 1982. Sand stresses around a wellbore. *Soc. Petrol. Eng. J.* 22(6), 883-898.

Saucier, R. J., 1974. Consideration in Gravel Pack Design, *J. Petrol. Technol.* 23(2), 205-212.

Schanz T., Vermeer P.A., Bonnier P.G., 1999. The hardening soil model: formulation and verification. Beyond 2000 in computational geotechnique – 10 Years of PLAXIS. Balkema, Rotterdam.

Shen, B., Stephansson, O., and Rinne, M., 2002. Simulation of borehole breakouts using FRACOD2D, *Oil. Gas. Sci. Technol. J.* 57(5), 579-590.

Tortike, W. S., 1991. Numerical simulation of thermal multiphase fluid flow in an elastoplastic deforming oil reservoir. (PhD Thesis). University of Alberta, Canada.

Tronvoll, J., Fjaer, E., 1994. Experimental study of sand production from perforation cavities. *Int. J. Rock. Mech. Min.* 31(5), 393-410.

Tsuji, Y., Kawaguchi, T., Tanaka, T., 1993. Discrete particle simulation of two-dimensional fluidized bed. *Power. Technol. 77*, 79-87.

Van den Hoek, P. J., Hertogh, G. M. M., Kooijman, A. P., Bree, Ph. De., Kenter, C. J., Papamichos, E., 2000. A New Concept of Sand Production Prediction: Theory and Laboratory Experiments. *SPE. Drill. Completion*. 15(4), 261-273.